





Induction of uniaxial anisotropy by controlled phase separation in Y-Co thin filmsS. Sharma ^{*}, D. Ohmer, A. Zintler, M. Major, I. Radulov , U. Kunz , P. Komissinskiy, B. Xu , H. Zhang, L. Molina-Luna, K. P. Skokov, and L. Alff[†]*Institute of Materials Science, Technische Universität Darmstadt, 64287 Darmstadt, Germany*

(Received 10 March 2020; revised 4 July 2020; accepted 6 July 2020; published 20 July 2020)

In this study, molecular beam epitaxy is utilized to stabilize a nanostructured thin-film magnet consisting of a soft magnetic Y_2Co_{17} exchange coupled to hard magnetic YCo_5 . While, typically, a phase decomposition can be obtained in rare-earth cobalt systems only by the addition of further elements like Cu, Fe, and Zr and complex heat treatments, here we directly induce phase separation by growth kinetics. The resulting nanoscale architecture, as revealed by cross-sectional transmission electron microscopy, is composed of a network of coherently interlinked and aligned Y_2Co_{17} and YCo_5 building blocks. The formation of coherent precipitations is facilitated by the perfectly matching lattice constants, atomic species, and crystal symmetry of the two phases with vastly different magnetocrystalline anisotropies. The hard magnetic phase induces an aligned uniaxial anisotropy in Y_2Co_{17} , resulting in substantial coercivity associated with enhanced energy products. This work highlights the importance of thin-film epitaxy in understanding magnetic hardening mechanisms and suggests strategies for a rational design of future sustainable magnetic systems.

DOI: [10.1103/PhysRevB.102.014435](https://doi.org/10.1103/PhysRevB.102.014435)**I. INTRODUCTION**

Research on magnetic materials is driven by the need to develop beyond state-of-the-art magnets which are key components of emerging green-energy technologies such as electric vehicles, wind turbines, and hydroelectric power generators [1]. For a material to qualify as a permanent magnet, a critical requirement is to have a strong uniaxial magnetocrystalline anisotropy in addition to a high Curie temperature and saturation magnetization [2]. There are numerous compounds which show an easy-plane anisotropy at room temperature such as all of the $R_2\text{Fe}_{17}$ (R is a rare-earth element) intermetallics and the $R_2\text{Co}_{17}$ compounds with a nonmagnetic rare-earth element [3]. The presence of an easy-plane anisotropy generally results in negligible coercivity in these compounds, as the magnetization rotates freely in the easy plane, thus rendering them ineffective as permanent magnets. The possibility to tune the anisotropy of materials from easy plane to uniaxial not only will broaden the class of materials useful for permanent magnet applications but also is beneficial for various research directions ranging from energy conversion to biotechnology [4–6].

Different methods have been proposed to induce uniaxial magnetocrystalline anisotropy. The first approach involves expansion of the crystal lattice through interstitial atoms like nitrogen or carbon [7,8]. However, the low diffusivity of N or C hinders the production of bulk magnets. So far, this approach has been successful in only a few material systems such as $\text{Sm}_2\text{Fe}_{17}\text{N}_3$ [9]. In the second approach, exchange interactions between crystallites of appropriate dimensions and orientations in nanostructured magnets result in an ef-

fective uniaxial anisotropy [10,11]. A strong exchange coupling requires proper structuring, alignment, and distribution of magnetic components at the nanoscale. Self-assembly of magnetically hard and soft phases is a potential way of not only overcoming the challenges of nanostructuring but also designing smart functional materials [12,13]. For example, self-organized assembly of exchange-coupled FePt and Fe_3Pt nanoparticles has shown to exceed the theoretically proposed energy product of noncoupled FePt [14,15]. In this work, we present a different approach in which a controlled phase separation in molecular beam epitaxy (MBE) is utilized to stabilize an exchange-coupled Y_2Co_{17} - YCo_5 nanostructured magnet. The two phases self-assemble in a way that results in a uniaxial anisotropy and an enhanced energy density without further elements that are necessary for the induction of phase decomposition, e.g., in the $\text{Sm}(\text{Co,Fe,Cu,Zr})_{7.5-8}$ system, which outperforms Nd-Fe-B magnets in high-temperature applications [16].

YCo_5 and Y_2Co_{17} are crystallographically coherent phases in which the CaCu_5 -type hexagonal ($P6/mmm$) structure of YCo_5 is the building block of Y_2Co_{17} , which has either a $\text{Th}_2\text{Ni}_{17}$ -type hexagonal ($P6_3/mmc$) or $\text{Th}_2\text{Zn}_{17}$ -type rhombohedral ($R\bar{3}m$) structure, as shown in Figs. 1(a)–1(c). There are no $4f$ electrons in yttrium, and the anisotropy of these intermetallics comes entirely from the cobalt $3d$ electrons. Polarized neutron diffraction results for YCo_5 have shown that $\text{Co}(2c)$ sites mainly contribute to the extremely large uniaxial magnetocrystalline anisotropy [18–21]. An excess of Co in Y_2Co_{17} (in the form of Co dumbbells) leads to a reduction in symmetry at the $\text{Co}(2c)$ site and thus to a reduced basal-plane anisotropy [22].

In Y_2Co_{17} -based bulk alloys, a uniaxial anisotropy and an improved coercivity achieved via precipitation hardening by the addition of Cu and Zr, Hf, or Ti and complex heat treatments were reported [23]. Thin-film fabrication techniques

^{*}shalini.sharma@tu-darmstadt.de[†]lambert.alf@tu-darmstadt.de

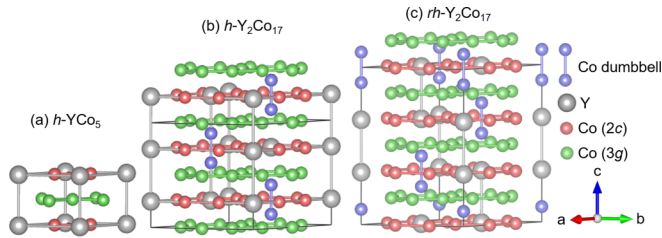


FIG. 1. Atomic arrangements in (a) CaCu_5 -type hexagonal (h) YCo_5 , (b) $\text{Th}_2\text{Ni}_{17}$ -type hexagonal (h) Y_2Co_{17} , and (c) $\text{Th}_2\text{Zn}_{17}$ -type rhombohedral (rh) Y_2Co_{17} ; crystal structures were created using the VESTA program [17].

not only allow stabilization of metastable phases and their crystallographic alignment but also provide a means to study the hardening mechanism in nanostructured magnets, which cannot be produced by conventional bulk methods.

The literature available on the development of rare-earth cobalt thin films using molecular beam epitaxy is quite limited, with the majority of work focused on the Sm-Co system [24–28]. In all these reports, additional buffer layers such as Ru, Co, Cr, and mostly Cu have been used either to stabilize the SmCo_5 phase or/and to promote a specific crystallographic texture. However, Cu diffuses into the Sm-Co layer and substitutes Co to form $\text{Sm}(\text{Co},\text{Cu})_5$ which lowers the saturation magnetization, Curie temperature and magnetocrystalline anisotropy of the pure SmCo_5 phase [29]. As previously reported in our earlier work based on Y-Co, Ce-Co, and Sm-Co thin films grown by MBE, we were able to stabilize the RCo_5 phase exhibiting a perpendicular magnetic anisotropy without any additional buffer layers [30–32]. In the Y-Co system, we observed a gradual transition from the Y_2Co_{17} to the YCo_5 phase on decreasing the Co evaporation rate [30]. In this paper, we describe the approach for fabricating self-assembled Y_2Co_{17} - YCo_5 nanostructured magnets by a controlled phase separation. A detailed analysis of the microstructure is additionally provided and correlated to the observed magnetic properties. Subsequently, micromagnetic simulations are used to understand the magnetization reversal process and study the interaction between the magnetic moments at the interface of two phases.

II. EXPERIMENT

The Y-Co thin films were grown on (001)-oriented single-crystalline Al_2O_3 substrates by molecular beam epitaxy. The substrates were annealed prior to deposition at 570°C for 30 min in vacuum in the MBE chamber. The films were grown by coevaporation of elemental Y (99.9% purity) and Co (99.95% purity) by electron beam at a base pressure of 10^{-8} mbar. The evaporation rate of the metals was monitored and controlled using a quartz crystal microbalance with a rate-deposition controller and a feedback loop. After deposition, the films were capped with Ag at room temperature using thermal evaporation to prevent oxidation. Crystallographic structural characterization was carried out by x-ray diffraction (XRD) using $\text{Cu } K_\alpha$ radiation with a Rigaku SmartLab system. A magnetic property measurement system (Quantum Design) equipped with a superconducting quantum interference de-

vice was used to perform the magnetization measurements with an applied magnetic field up to 6 T. Angle-dependent torque measurements were carried out in a physical property measurement system (Quantum Design) with an additional torque magnetometry option. Bright- and high-angle annular dark-field scanning transmission electron microscopy (BF and HAADF STEM) was performed on a JEOL JEM-ARM 200F microscope operated at 200-kV acceleration voltage. Energy dispersive x-ray spectroscopy (EDS) maps were recorded with a JEOL JED-2300T EDS detector. Gatan Digital Micrograph's internal Cliff-Lorimer K -factor quantification was used. Approximately 300 nm of Au were sputtered on top of the films to protect them during the lamella preparation by focused ion beam. The multislice simulations of the HAADF STEM images were carried out using DR. PROBE software [33].

In this work, bulk single crystals of Y_2Co_{17} and YCo_5 in the form of spheres were also synthesized. The ingots were prepared by induction melting of mixtures of Y and Co in Alundum crucibles in Ar atmosphere. The mixture was rapidly heated up to the melting point and subsequently cooled down at a rate of 60–80 K/min. The obtained ingots were homogenized for 1 week at 1050°C and then broken. The large grains were shaped into spheres using a grinding wheel. The strained surface layer was removed by electrochemical polishing in a saturated solution of CrO_3 in orthophosphoric acid. The crystal orientation was confirmed by means of the x-ray back Laue diffraction method.

The micromagnetic simulations of model Y_2Co_{17} - YCo_5 nanocomposites were performed using the three-dimensional NIST Object Oriented Micromagnetic Framework (OOMMF) code [34]. A discretization cell size of 1 nm was chosen so that it was smaller than the domain wall width δ_w and the exchange length δ_{ex} of Y_2Co_{17} and YCo_5 .

III. RESULTS AND DISCUSSION

A. Controlled phase separation

In R_2M_{17} pinning-type magnets, a disordered R_2M_{17} or RM_7 phase is considered to decompose into ordered R_2M_{17} and RM_5 phases, which results in precipitation hardening [35,36]. In order to establish the phase decomposition reaction in thin films, first, the growth window for the Y_2Co_{17} phase is identified, and then, the YCo_5 phase is approached with increasing Y content (evaporation rate).

Figure 2(a) shows the XRD patterns of the Y-Co thin films grown at 590°C with an increasing ratio of evaporation rates of Y to Co from bottom to top. The Co rate is kept constant at 0.25 \AA/s , while the Y rate is increased from 0.18 to 0.25 \AA/s . The films are about 30 nm thick. The reflections corresponding to the 006 Al_2O_3 substrate at 41.67° (along with its lower- and higher-order peaks) and 111 Ag cap layer at 38.18° are marked by asterisks and the plus sign, respectively.

A magnified view of the diffraction peaks of the intermetallic compounds between 42.9° and 46° is shown in Fig. 2(b). The (001)-oriented Al_2O_3 substrate promotes the growth of c -axis textured films, as indicated by the appearance of 00/ reflections. For the films grown with Y to Co ratios of 0.72 and 0.80, the Y_2Co_{17} phase is formed. The peak at approximately 44° corresponds to the 004 reflection of the hexagonal Y_2Co_{17}

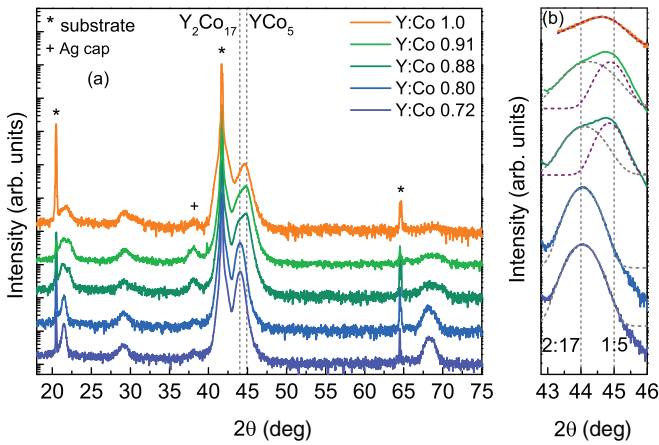


FIG. 2. (a) X-ray diffraction patterns of Y-Co thin films grown onto (001)-oriented Al_2O_3 substrates at 590°C with an increasing ratio of evaporation rate of Y to Co from bottom to top. The rate of Y is increased from 0.18 to 0.25 $\text{\AA}/\text{s}$, while the Co rate is fixed at 0.25 $\text{\AA}/\text{s}$. (b) Magnified view of the film peaks (in logarithmic scale) between 42.9° and 46° with fitting using the Gaussian distribution function. The positions of the 004 Y_2Co_{17} (2:17) and 002 YCo_5 (1:5) Bragg reflections are marked by vertical dashed lines.

phase [37]. It is symmetric, and a single Gaussian distribution function is used to fit the peak. The lower-order 002 and higher-order 006 reflections are also observed at 21° and 68° , respectively.

With an increase in the Y to Co ratio between 0.88 and 0.91, the peak at 45° , corresponding to the 002 reflection of the YCo_5 phase, is additionally observed [37]. In this case, the region between 42.9° and 46° is fit with two Gaussian peaks. At these growth conditions, both Y_2Co_{17} and YCo_5 phases are stabilized simultaneously. For these films, a doubling of the lower-order peak around 21° and a broad higher-order reflection around 68° are also observed. With a further increase in the Y to Co ratio to 1, a single asymmetric peak slightly shifted from the 002 reflection of the hexagonal YCo_5 phase is observed. Additionally, traces of Y_2O_3 at 29° are observed in all of the films.

We observed that at intermediate compositions, a natural phase decomposition during the film growth results in a separation and stabilization of both Y_2Co_{17} and YCo_5 phases simultaneously. The (001)-oriented Al_2O_3 substrate imposes a crystalline order onto the nanocomposite film such that crystallographic c axes of Y_2Co_{17} and YCo_5 phases are parallel to each other, favoring coherent growth.

The average grain size of the Y_2Co_{17} ($d_{2:17}$) and YCo_5 ($d_{1:5}$) phases in the nanocomposite film is estimated from the width of the 004 reflection of Y_2Co_{17} and the 002 reflection of YCo_5 , using the Scherrer equation given by

$$d = (0.9\lambda)/[\beta \cos(\theta)],$$

where λ is the wavelength of Cu K_α x-ray radiation and β represents the full width at half maximum. The grain sizes are provided in Table I.

It can be seen that the average grain size of the Y_2Co_{17} and YCo_5 phases in the films is in the range of 5–15 nm. Such nanoscale dimensions of the two phases are considered

TABLE I. Average grain size of the Y_2Co_{17} ($d_{2:17}$) and YCo_5 ($d_{1:5}$) phases in the nanocomposite films as estimated by the Scherrer equation.

Rate ratio (Y:Co)	$d_{2:17}$ (nm)	$d_{1:5}$ (nm)	Size ratio ($d_{2:17}:d_{1:5}$)
0.88	7.33	11.13	0.658
0.91	5.87	10.44	0.563

favorable for an effective exchange coupling as exchange is a short-range interaction [38]. The effect of the phase space of Y_2Co_{17} exchange coupled to the YCo_5 phase on the magnetic properties is described in detail using micromagnetic simulations in Sec. III G.

B. Microstructure of an Y_2Co_{17} - YCo_5 nanocomposite film

A cross-sectional high-resolution HAADF STEM image of the Y_2Co_{17} - YCo_5 nanocomposite film grown at a Y to Co rate ratio of 0.91 on a (001)- Al_2O_3 substrate is shown in Fig. 3(a). The cross section was cut along the [100] zone axis of the Al_2O_3 substrate in order to achieve on-axis observation conditions for high-resolution imaging.

The film has regions with well-defined atomic contrast and highly crystalline structure. The inset shows a magnified view of the indicated area. In order to confirm the phase of the crystalline layer, multislice simulations were carried out. Figure 3(b) shows a simulated image of the YCo_5 phase viewed along the [100] direction, and Fig. 3(c) shows a simulated image of the Y_2Co_{17} phase viewed along the [210] direction. For both phases, the c axes are parallel to the film growth direction. As a model structure, a supercell of the two phases was created, preserving the projection orientation. The supercell represents a stack of equal-volume ratio of 1:5 and 2:17 unit cells, resulting in the micrograph shown in Fig. 3(d). The generated image matches well with the experimental STEM image of the film shown in Fig. 3(e), thus supporting the nanocomposite nature of the film.

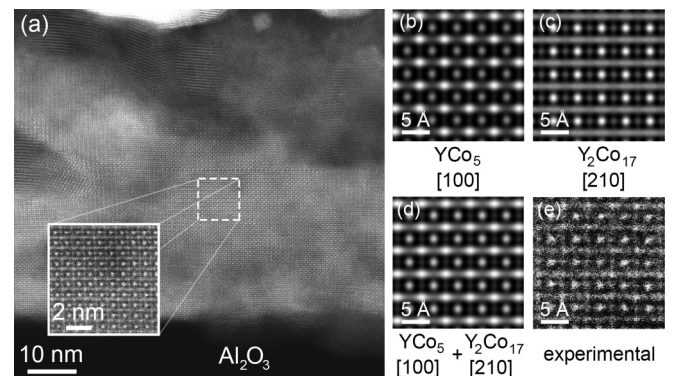


FIG. 3. (a) Cross-sectional high-resolution HAADF STEM image of the Y_2Co_{17} - YCo_5 nanocomposite film grown on a (001)-oriented Al_2O_3 substrate at 590°C . Multislice simulations of a 15-nm slab of (b) YCo_5 crystal viewed along the [100] direction, (c) Y_2Co_{17} crystal along the [210] viewing direction, and (d) a supercell of combined YCo_5 [100] and Y_2Co_{17} [210] cells. (e) Experimental atomic-resolution HAADF STEM image of the crystalline area marked in (a).

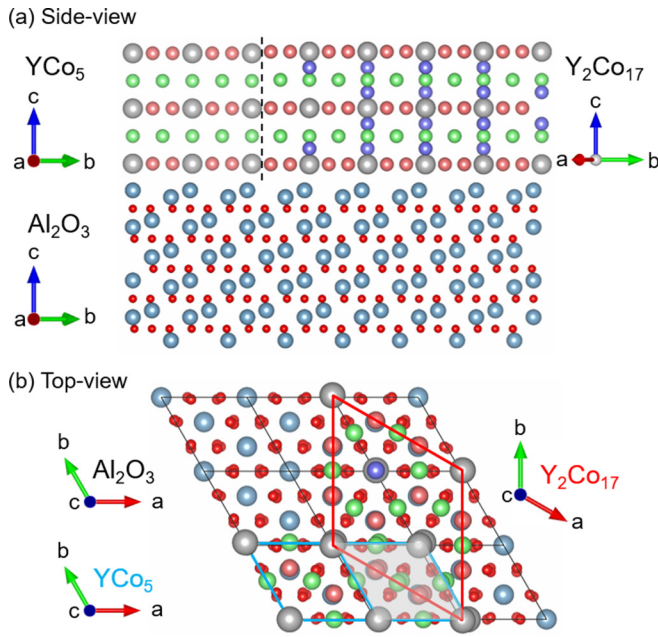


FIG. 4. Schematic representation of the epitaxial arrangement of YCo₅ and Y₂Co₁₇ crystal structures on top of Al₂O₃ unit cells, showing the coherency of interfaces (a) along the *c* axis by a vertical dashed line and (b) in the *a-b* plane by the shaded area. Refer to Fig. 1 for the color coding of Y and Co atoms of the YCo₅ and Y₂Co₁₇ structures. The Al and O atoms of the substrate are in light blue and red, respectively.

The here-described nanostructured magnet comprises coherently interlinked Y₂Co₁₇ and YCo₅ building blocks with the observed microstructure formed as a result of thin-film growth kinetics and epitaxy.

As seen in the yttrium rate scan shown in Fig. 2, the nanocomposite film is formed at compositions in between Y₂Co₁₇ and YCo₅ phases. Such intermediate compositions is one of the main factors which drive the decomposition of the pinning-type Sm(Co,Fe,Cu,Zr)_{7.5–8} magnets. Thus, at the employed growth conditions of the film, with a supply of sufficient Y and Co atoms, the nucleation of both Y₂Co₁₇ and YCo₅ occurs simultaneously, while their crystallographic alignment on the substrate is governed by the thin-film epitaxy.

The arrangement of the Y₂Co₁₇ and YCo₅ crystal structures on top of Al₂O₃ unit cells is schematically represented in Fig. 4. As can be seen in the side-view image [Fig. 4(a)], the (001)-oriented Al₂O₃ (trigonal lattice) directs a parallel alignment of the *c* axes of the hexagonal Y₂Co₁₇ and YCo₅ structures normal to the film plane, i.e., Y₂Co₁₇ (001) || Al₂O₃ (001) and YCo₅ (001) || Al₂O₃ (001). A coherent interface between the YCo₅ and Y₂Co₁₇ phases along the *c* axis is shown by a vertical dashed line.

In the *a-b* plane [Fig. 4(b)], a single unit cell of YCo₅ (blue) is oriented in the same way as the Al₂O₃ unit cell (black), while Y₂Co₁₇ (red) is rotated by 30°, i.e., YCo₅ [100] || Al₂O₃ [100] and Y₂Co₁₇ [210] || Al₂O₃ [100]. Such epitaxial relations result in a lattice mismatch of 4.02% for YCo₅ and 1.43% for Y₂Co₁₇. The shaded area represents an overlay of Y₂Co₁₇ and YCo₅ crystal structures, showing the aptly fitting

length scales in the two phases. Thus, closely matching lattice parameters, chemical species, and crystal symmetry of the Y₂Co₁₇ and YCo₅ phases give rise to a coherent nanoscale architecture of the film.

C. Easy-plane anisotropy in Y₂Co₁₇ thin films

The magnetic hysteresis curves were measured in two directions, in the plane (IP, gray diamonds) and out of the plane (OP, orange spheres) of the film surface at room temperature, as shown in Fig. 5.

The Y₂Co₁₇ film [Fig. 5(a)] is characterized by a soft ferromagnetic behavior with a maximum magnetization of 772.63 kA/m and a small coercivity. The shape of the curves suggests that the easy direction of magnetization lies in the film plane, while the hard axis is perpendicular to it, in agreement with the in-plane anisotropy observed in W-buffered Y₂Co₁₇ films [39]. The observed easy-plane anisotropy is governed by the shape anisotropy due to a dominating magnetostatic energy contribution. The initial magnetization curve of the film is shown in the inset of Fig. 5(a). A steep rise in the magnetization under a small applied field shows that the domain walls move easily, resulting in a high permeability. Such behavior is attributed to nucleation-controlled reversal of magnetization.

The effect of the shape anisotropy can be excluded in spherical crystals, and therefore, to determine the magnetocrystalline anisotropy of the Y₂Co₁₇ and YCo₅ phases, the magnetization of bulk single crystals is measured, as shown in Fig. 6. The magnetization is measured perpendicular (⊥) and parallel (||) to the crystallographic *c* axis at room temperature. In Y₂Co₁₇ (red), an easy-plane anisotropy of -0.33 MJ/m³ is determined from the anisotropy field.

D. Perpendicular anisotropy in YCo₅ thin films

The hysteresis curves of the YCo₅ film, measured IP (gray diamonds) and OP (orange spheres) of the film surface, are shown in Fig. 5(b). The YCo₅ film is magnetically hard with a magnetization of 610.98 kA/m. It can be seen that the hysteresis measured perpendicular to the film plane is larger than the in-plane hysteresis and has a higher remanence and coercivity, indicating that the major component of magnetization is normal to the film plane.

The magnetization curves of single crystals of YCo₅ (blue) are shown in Fig. 6. A uniaxial anisotropy of 5.5 MJ/m³ is measured with the easy axis of magnetization parallel to the *c* axis of the hexagonal crystal. Thus, the *c*-axis textured growth of the YCo₅ phase with magnetocrystalline anisotropy exceeding the shape anisotropy of the film results in a predominantly perpendicular orientation of magnetization.

To understand the origin of coercivity of the YCo₅ film, its microstructure was investigated using STEM, as shown in Fig. 7. The composition integrated over the full layer refers to an atomic percent of Y of $17.57\% \pm 0.26\%$ and Co of $82.43\% \pm 0.28\%$, corresponding to YCo₅. An overview of the film morphology reveals an intricate microstructure. The single-crystal Al₂O₃ substrate enables a layer-by-layer growth of highly crystalline YCo₅ up to a thickness of 10 nm. With increasing thickness, the layer-by-layer growth turns

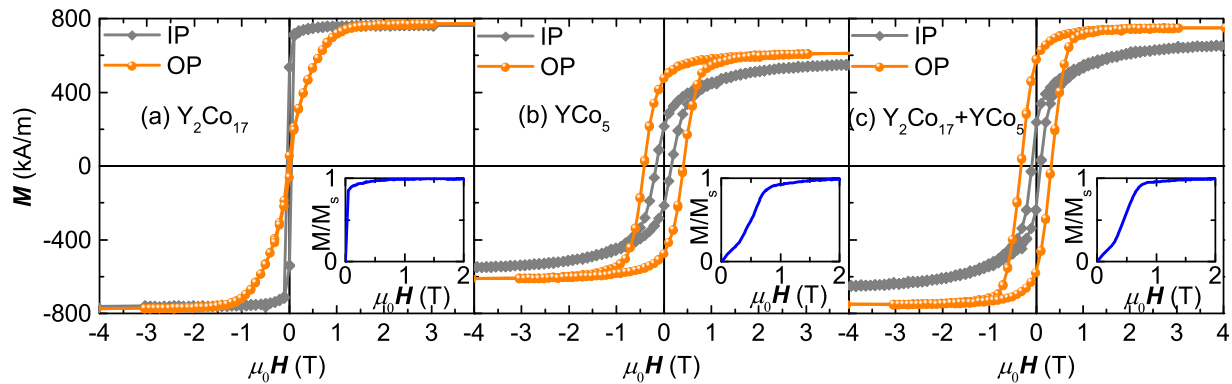


FIG. 5. Room-temperature hysteresis curves of (a) an Y_2Co_{17} film, (b) an YCo_5 film, and (c) an Y_2Co_{17} - YCo_5 nanocomposite film, measured in the plane (IP, gray diamonds) and out of the plane (OP, orange spheres) of the film surface. The corresponding initial magnetization curves are shown in the insets.

into an island-type growth of yttrium-deficient YCo_5 grains. The grains are c axis textured, however, with stacking faults as indicated by the vertical lines in the fast Fourier transformation shown in the inset of Fig. 7. The narrow thermodynamic stability of YCo_5 and epitaxial and/or thermal strain, accompanied by the strong oxygen affinity of Y, lead to the growth of a defect-rich YCo_5 phase in the grains.

From the magnetic point of view, the microstructure of the film is made up of a single-crystalline layer as well as about 40-nm-sized grains of highly anisotropic YCo_5 . The initial magnetization curve of the YCo_5 film, in the inset of Fig. 5(b), shows a gradual rise of magnetization with applied field. Such a switching behavior was observed, e.g., in FePt films with single-domain or mesoscopic islands in which the magnetization reversal takes place by a coherent or incoherent rotation process [40,41]. According to the Stoner-Wohlfarth model, large fields of the order of the anisotropy field are required to bring remanent magnetization to zero; however, the presence of stacking faults or other types of defects in the grain leads to reduced coercivity. The disordering of crystal planes in the film growth direction results in a deviation of the c axis and hence a reduced perpendicular magnetic anisotropy of the film compared to the uniaxial magnetocrystalline anisotropy.

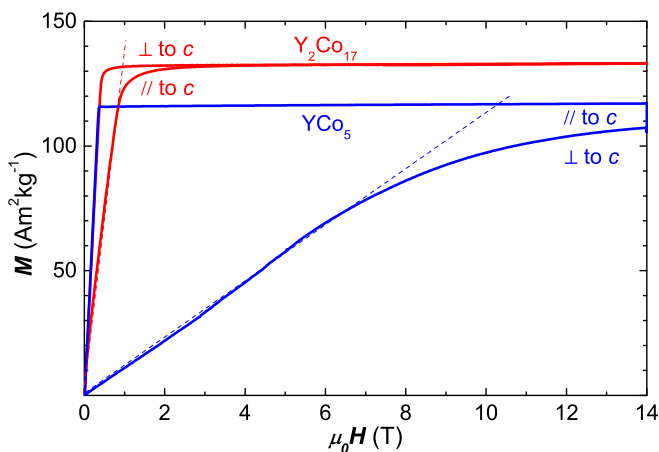


FIG. 6. Room-temperature magnetization curves of bulk single crystals of Y_2Co_{17} (red) and YCo_5 (blue) measured parallel (\parallel) and perpendicular (\perp) to the c axis.

E. Perpendicular anisotropy in the Y_2Co_{17} - YCo_5 nanocomposite film

Now, we describe the magnetic properties of the nanocomposite film of soft magnetic Y_2Co_{17} and hard magnetic YCo_5 . The corresponding hysteresis curves measured at room temperature, parallel and perpendicular to the film plane, are shown in Fig. 5(c). Similar to the YCo_5 film, the nanocomposite film also shows perpendicular anisotropy. There is an overall enhancement in the remanence compared to YCo_5 , as well as in the coercivity compared to Y_2Co_{17} . Since the magnetocrystalline anisotropy of the Y_2Co_{17} phase is small, its magnetization is pinned to the highly anisotropic phase of YCo_5 , leading to a hard magnetic behavior. The hysteresis curves measured in both the directions are continuous without a kink, indicating a strong exchange interaction between the phases. The grain size of the Y_2Co_{17} phase (Table I) is less than twice the domain-wall thickness of YCo_5 (5.5 nm [42]) in both of the nanocomposite films. Such nanoscale architecture of the film enables an effective exchange coupling, well in agreement with the exchange-hardening mechanism proposed for nanostructured two-phase magnets [43,44].

The initial magnetization of the film, shown in the inset of Fig. 5(c), rises gradually with the applied magnetic field. The Y_2Co_{17} - YCo_5 nanocomposite film shows gradually varying structural and magnetic properties. The gradients in concentration, as well as alterations of both anisotropy and

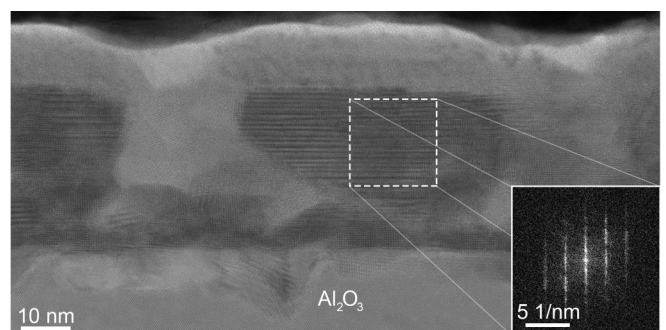


FIG. 7. The cross-sectional BF image of the YCo_5 film grown on the (001)-oriented Al_2O_3 substrate. The inset shows the fast Fourier transformation map of the YCo_5 grain.

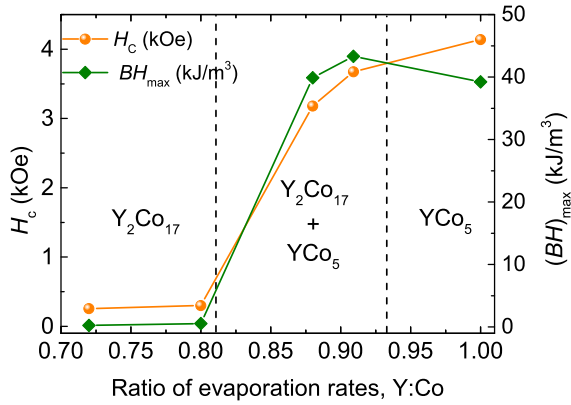


FIG. 8. Coercive field H_c and maximum energy product $(BH)_{\max}$ versus the ratio of evaporation rates of Y to Co in Y-Co thin films. The three regions correspond to the growth of Y_2Co_{17} , YCo_5 , and a nanocomposite of Y_2Co_{17} and YCo_5 phases.

exchange energies, change the energy of the domain wall and hence hinder its motion, pointing towards a pinning-controlled coercivity mechanism.

The conventional pinning-type $Sm(Co,Fe,Cu,Zr)_{7.5-8}$ magnets upon thermal decomposition and complex heat treatments yield an ordered cellular structure of $Sm(Co,Cu)_5$, $Sm_2(Co,Fe)_{17}$, and $Sm(Co,Fe,Cu,Zr)_{10-11}$ phases with parallel c axes [16,36]. In the present study, a controlled phase separation, governed by the thin-film growth kinetics and epitaxy, leads to coherent interfaces between Y_2Co_{17} and YCo_5 crystal structures. For a favorable exchange coupling, the dimensions as well as the crystallographic texture of the soft and hard magnetic phases are important. In the nanocomposite film described here, as the size of the Y_2Co_{17} phase is of the order of (or slightly exceeds) the exchange length, the magnetization of each phase of either Y_2Co_{17} or YCo_5 is influenced by the presence of the other. Due to the exchange interaction, the magnetization of the Y_2Co_{17} phase is driven out of its easy basal plane and gets aligned with the easy axis of magnetization of the highly anisotropic YCo_5 phase.

F. Composition dependence on coercivity and the maximum energy product

A plot of the composition dependence of the coercive field H_c and the maximum energy product $(BH)_{\max}$ measured perpendicular to the film plane is shown in Fig. 8. Here vertical dashed lines mark different regions corresponding to Y_2Co_{17} , YCo_5 , and a nanocomposite of Y_2Co_{17} and YCo_5 phases.

The Y_2Co_{17} films are soft magnetic with a small coercivity and energy product. Then, there is a sharp increase in the coercivity and energy product in the nanocomposite, where both the Y_2Co_{17} and YCo_5 phases coexist as a magnetically exchange coupled system. The combination of a high magnetization of Y_2Co_{17} and a large coercivity of YCo_5 gives rise to the peak in $(BH)_{\max}$. The third region corresponds to the YCo_5 film with the highest coercivity of 4.14 kOe. The film exhibits $(BH)_{\max}$ of 39.22 kJ/m³, which is the highest reported so far for thin films and is comparable to melt-spun ribbons and ball-milled nanopowders [28,45–47].

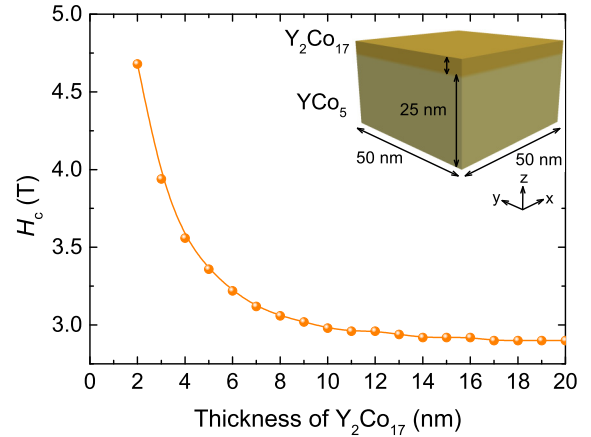


FIG. 9. Coercive field H_c of a model Y_2Co_{17} - YCo_5 nanocomposite as a function of Y_2Co_{17} thickness for magnetic field applied in the z direction. The inset shows an example geometry with a 5-nm Y_2Co_{17} layer on top of YCo_5 .

Thus, the coercivity increases from the Y_2Co_{17} to the YCo_5 film, while a maximum in $(BH)_{\max}$ is obtained in the Y_2Co_{17} - YCo_5 nanostructured magnet. The observed pinning mechanism, arising from the local change in anisotropy and composition, in combination with high magnetization of the Y_2Co_{17} phase, leads to an enhanced energy density without the need for additional elements.

G. Micromagnetic simulation of the Y_2Co_{17} - YCo_5 nanocomposite

In this section, micromagnetic simulations are utilized to study the interaction between the magnetic moments in the Y_2Co_{17} and YCo_5 phases at the interface and understand the magnetization reversal process in a nanocomposite of the two phases. The experimentally measured saturation magnetization M_S and magnetocrystalline anisotropy of the single crystals of Y_2Co_{17} and YCo_5 are used. M_S of Y_2Co_{17} is 994.48 kA/m, and it shows an easy-plane anisotropy of -0.33 MJ/m³. On the other hand, M_S of YCo_5 is 865.45 kA/m, and it exhibits a uniaxial anisotropy of 5.5 MJ/m³. The exchange stiffnesses A for Y_2Co_{17} and YCo_5 are taken to be 12 and 9.4 pJ/m, respectively [48]. The exchange lengths ($\delta_{ex} = \sqrt{\frac{2A}{\mu M_S^2}}$) of Y_2Co_{17} and YCo_5 are calculated to be 4.39 and 4.47 nm, respectively.

The nanocomposite geometry used for simulations is made up of a bottom layer of YCo_5 (area of 50×50 nm²) in contact with a top layer of Y_2Co_{17} of varying thickness. An example geometry with a 5-nm Y_2Co_{17} layer is shown in the inset of Fig. 9. The crystallographic c axes of both the phases are aligned along the z direction. While the easy axis of magnetization of YCo_5 is parallel to the z direction, Y_2Co_{17} shows easy-plane anisotropy with the xy plane as the easy plane. From the experiments, the average grain size of the Y_2Co_{17} phase in the nanocomposite film, exhibiting the highest $(BH)_{\max}$, is determined to be 5.87 nm. Here we first describe the evolution of magnetization with applied field for a 5-nm-thick layer of Y_2Co_{17} on top of YCo_5 . Second, we

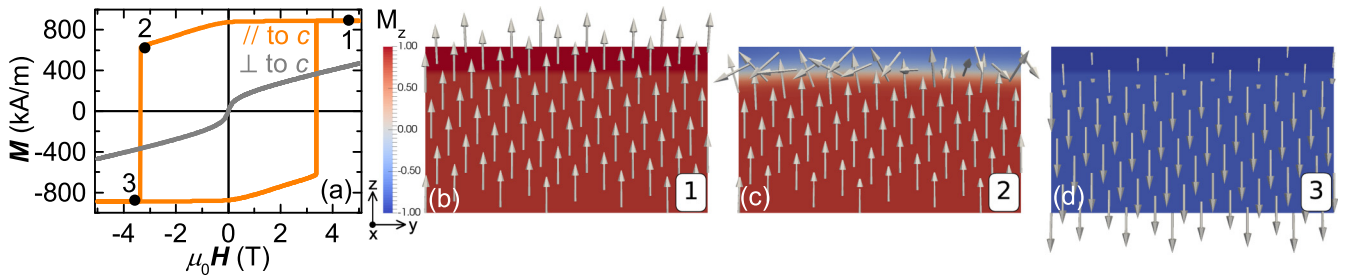


FIG. 10. (a) The simulated magnetization curves of a model Y_2Co_{17} - YCo_5 nanocomposite with a 5-nm layer of Y_2Co_{17} on top of 25 nm of YCo_5 when the field is applied parallel and perpendicular to the c axis. Evolution of magnetization during the reversal process at (b) 5 T, (c) -3.36 T, and (d) -3.38 T.

investigate the influence of the thickness of the Y_2Co_{17} layer (from 2 to 20 nm) on the coercivity of the nanocomposite.

Figure 10(a) shows the simulated magnetization curves with the external magnetic field applied parallel and perpendicular to the c axes of both the phases. Color-coded maps of the z component of magnetization M_z during the magnetization reversal process are shown in Figs. 10(b)–10(d). The arrows represent the direction of magnetization in the individual phases.

At the maximum field of 5 T applied along the z direction of the nanocomposite [indicated by 1 in Fig. 10(a)], saturation magnetization is achieved. As can be seen in Fig. 10(b), the magnetization vectors in both the phases are oriented along the external field direction. However, a field of 5 T is not sufficient to reach saturation magnetization in a direction perpendicular to the c axis. This shows that the easy axis of magnetization of the nanocomposite is aligned parallel to the c axis and the hard axis is normal to it, which is in agreement with the perpendicular anisotropy experimentally observed in the nanocomposite thin film.

When the direction of the field is reversed [indicated by 2 in Fig. 10(a)], the magnetization reversal process begins in the Y_2Co_{17} as it has a smaller anisotropy. The slope in the magnetization curve arises because of the rotation of moments in the Y_2Co_{17} phase, as well as in the top YCo_5 layer close to the interface. As can be seen in Fig. 10(c), the magnetization vectors in the Y_2Co_{17} and top layer of YCo_5 rotate and orient with the field, while the magnetization vectors in the YCo_5 phase that are away from the interface remain aligned along its easy axis until the coercive field is reached.

At the coercive field [indicated by 3 in Fig. 10(a)], the magnetization of the Y_2Co_{17} layer as well as the entire YCo_5 layer is fully reversed. As can be seen in Fig. 10(d), the magnetization vectors in the Y_2Co_{17} and YCo_5 layers are aligned with the external field again (in the negative z direction).

The coercive field of the model Y_2Co_{17} - YCo_5 nanocomposite is plotted as a function of the thickness of the Y_2Co_{17} layer in Fig. 9. Note that the coercivity is derived from the sum of the contributions from the exchange, anisotropy, and demagnetization energy. The latter strongly depends on the shape and size of the model, and therefore, in this study, the trends observed with the thickness of the Y_2Co_{17} layer are of higher importance than the absolute values.

It can be seen that the coercivity decreases exponentially with increasing thickness of the soft magnetic Y_2Co_{17} phase

and saturates for layers thicker than 12 nm. This behavior is explained by considering the high magnetization of Y_2Co_{17} and the large anisotropy of YCo_5 . Depending on the thickness of the Y_2Co_{17} layer, the following three cases are described:

(a) When the thickness of the Y_2Co_{17} layer is less than the exchange length, its magnetization is strongly influenced by the YCo_5 phase, which has a 16 times larger magnetocrystalline anisotropy and is responsible for the high coercivity. Before the coercive field is reached, the magnetization vectors in the Y_2Co_{17} layer as well as in the top layer of YCo_5 (at the interface) rotate slowly towards the external field. As soon as the entire YCo_5 phase switches (at the coercive field), the magnetization vectors in the Y_2Co_{17} are aligned with the YCo_5 phase along the external field direction.

(b) When the thickness of the Y_2Co_{17} layer is in the range of the exchange length, the YCo_5 phase becomes less dominant, and the influence of the Y_2Co_{17} layer on the switching behavior in the YCo_5 phase increases. This means that the magnetization vectors in the YCo_5 phase, not only at the interface but deeper into the layer, rotate with the Y_2Co_{17} layer at reverse fields less than the coercive field. Therefore, the soft magnetic character of the Y_2Co_{17} reduces the barrier for switching the magnetization in the rest of the YCo_5 phase; that is, it reduces the overall coercivity.

(c) When the Y_2Co_{17} layer thickness is two or more times the exchange length, the coercivity reaches a saturation, as the volume of Y_2Co_{17} and YCo_5 interacting with each other no longer changes. The effect on the magnetization of an individual phase because of the presence of the other phase is strong only at a certain distance from the interface, given by the exchange length. Thus, the increasing thickness of the Y_2Co_{17} layer no longer influences the overall switching behavior of the nanocomposite.

IV. CONCLUSION

Thin-film fabrication methods provide a nonequilibrium means to control and design magnetic materials at the nanoscale and validate novel hardening mechanisms. In this work, the technique of molecular beam epitaxy is utilized to stabilize a self-assembled nanocomposite of soft magnetic Y_2Co_{17} and hard magnetic YCo_5 phases with enhanced energy density. The nanostructured magnet consists of coherently interlinked Y_2Co_{17} and YCo_5 structures with a c -axis-oriented growth texture induced by the substrate. A natural phase decomposition during the film growth results in a

controlled phase separation, with the grain size of Y_2Co_{17} on the order of the exchange length. Y_2Co_{17} thin films have an easy-basal-plane anisotropy, while YCo_5 thin films show a perpendicular magnetic anisotropy. As a result of the exchange interaction, the nanocomposite thin film of the two phases exhibits the desired perpendicular anisotropy. The pinning mechanism is the local change in anisotropy and composition on the nanoscale which in combination with the increased total magnetization due to the Co rich phase yields an enhanced energy product of the nanocomposite.

ACKNOWLEDGMENTS

Financial support from the Deutsche Forschungsgemeinschaft (DFG, German Research Foundation) Project ID 405553726-TRR 270, DFG Project ID MO 3010/3-1, Deutscher Akademischer Austauschdienst (DAAD), the LOEWE project RESPONSE, and the European Research Council (ERC) Horizon 2020 Program under Grant No. 805359-FOXON is acknowledged. The authors also acknowledge the access to the Lichtenberg High Performance Computer of Technische Universität Darmstadt.

-
- [1] O. Gutfleisch, J. P. Liu, M. Willard, E. Brück, C. Chen, and S. G. Shankar, *Adv. Mater.* **23**, 821 (2011).
- [2] M. D. Kuz'min, K. P. Skokov, H. Jian, I. Radulov, and O. Gutfleisch, *J. Phys.: Condens. Matter* **26**, 064205 (2014).
- [3] J. E. Greedan and V. U. S. Rao, *J. Solid State Chem.* **6**, 387 (1973).
- [4] J. Lee, J. Jang, J. Choi, S. Moon, S. Noh, J. Kim, J. Kim, I. Kim, K. Park, and J. Cheon, *Nat. Nanotechnol.* **6**, 418 (2011).
- [5] F. X. Redl, K. S. Cho, C. B. Murray, and S. O'Brien, *Nature (London)* **423**, 968 (2003).
- [6] J. Kim, S. Chung, S. Choi, H. Lee, J. Kim, and S. Kwon, *Nat. Mater.* **10**, 747 (2011).
- [7] J. M. D. Coey and H. Sun, *J. Magn. Magn. Mater.* **87**, L251 (1990).
- [8] J. M. D. Coey, H. Sun, Y. Otani, and D. P. F. Hurley, *J. Magn. Magn. Mater.* **98**, 76 (1991).
- [9] S. Brennan, R. Skomski, O. Cugat, and J. Coey, *J. Magn. Magn. Mater.* **140–144**, 971 (1995).
- [10] B. Balasubramanian, P. Manchanda, R. Skomski, P. Mukherjee, S. R. Valloppilly, B. Das, G. C. Hadjipanayis, and D. J. Sellmyer, *Appl. Phys. Lett.* **108**, 152406 (2016).
- [11] J. Fischbacher, A. Kovacs, H. Oezelt, M. Gusenbauer, D. Suess, and T. Schrefl, *Appl. Phys. Lett.* **111**, 192407 (2017).
- [12] D. J. Sellmyer, *Nature (London)* **420**, 374 (2002).
- [13] Z. Li, F. Yang, and Y. Yin, *Adv. Funct. Mater.* **30**, 1903467 (2020).
- [14] H. Zeng, J. Li, J. P. Liu, Z. L. Wang, and S. Sun, *Nature (London)* **420**, 395 (2002).
- [15] S. Sun, *Adv. Mater.* **18**, 393 (2006).
- [16] M. Duerrschabel, M. Yi, K. Uestuener, M. Liesegang, M. Katter, H. J. Kleebe, B. Xu, O. Gutfleisch, and L. Molina-Luna, *Nat. Commun.* **8**, 54 (2017).
- [17] K. Momma and F. Izumi, *J. Appl. Crystallogr.* **44**, 1272 (2011).
- [18] J. Schweizer and F. Tasset, *J. Phys. F* **10**, 2799 (1980).
- [19] G. Asti, F. Bolzoni, D. Melville, and S. Rinaldi, *IEEE Trans. Magn.* **11**, 1437 (1975).
- [20] W. G. D. Frederick and M. Hoch, *IEEE Trans. Magn.* **10**, 733 (1974).
- [21] J. Wernick and S. Geller, *Acta Crystallogr.* **12**, 662 (1959).
- [22] G. Hoffer and K. J. Strnat, *IEEE Trans. Magn.* **2**, 487 (1966).
- [23] A. M. Gabay, Y. Zhang, and G. C. Hadjipanayis, *J. Appl. Phys.* **90**, 882 (2001).
- [24] Y. Nukaga, M. Ohtake, F. Kirino, and M. Futamoto, *IEEE Trans. Magn.* **44**, 2891 (2008).
- [25] M. Ohtake, Y. Nukaga, F. Kirino, and M. Futamoto, *J. Cryst. Growth* **311**, 2251 (2009).
- [26] M. Ohtake, Y. Nukaga, F. Kirino, and M. Futamoto, *J. Appl. Phys.* **107**, 09A706 (2010).
- [27] T. Yanagawa, Y. Hotta, M. Yamada, M. Ohtake, F. Kirino, and M. Futamoto, *J. Appl. Phys.* **115**, 17A759 (2014).
- [28] M. Yamada, Y. Hotta, M. Ohtake, M. Futamoto, F. Kirino, and N. Inaba, *J. Magn. Soc. Jpn.* **40**, 132 (2016).
- [29] E. Lectard, C. H. Allibert, and R. Ballou, *J. Appl. Phys.* **75**, 6277 (1994).
- [30] S. Sharma, E. Hildebrandt, S. U. Sharath, I. Radulov, and L. Alff, *J. Magn. Magn. Mater.* **432**, 382 (2017).
- [31] S. Sharma, E. Hildebrandt, M. Major, P. Komissinskiy, I. Radulov, and L. Alff, *J. Magn. Magn. Mater.* **452**, 80 (2018).
- [32] S. Sharma, I. Radulov, M. Major, and L. Alff, *IEEE Trans. Magn.* **54**, 1 (2018).
- [33] J. Barthel, *Ultramicroscopy* **193**, 1 (2018).
- [34] M. J. Donahue and D. G. Porter, OOMMF software package, <http://math.nist.gov/oommf>.
- [35] A. E. Ray, *J. Appl. Phys.* **55**, 2094 (1984).
- [36] L. Rabenberg, R. K. Mishra, and G. Thomas, *J. Appl. Phys.* **53**, 2389 (1982).
- [37] International Center for Diffraction Data (ICDD), PDF 04-001-1972. S. Gates-Rector and T. Blanton, *Powder Diffr.* **34**, 352 (2019).
- [38] X. K. Sun, J. Zhang, Y. Chu, W. Liu, B. Cui, and Z. Zhang, *Appl. Phys. Lett.* **74**, 1740 (1999).
- [39] F. Robaut, P. Milkulik, N. Chierief, O. F. K. McGrath, and D. Givord, *J. Appl. Phys.* **78**, 997 (1995).
- [40] T. Shima, K. Takanashi, Y. K. Takahashi, and K. Hono, *Appl. Phys. Lett.* **85**, 2571 (2004).
- [41] C. Behler, V. Neu, L. Schultz, and S. Fähler, *J. Appl. Phys.* **112**, 083919 (2012).
- [42] J. D. Livingston and M. D. McConnell, *J. Appl. Phys.* **43**, 4756 (1972).
- [43] E. F. Kneller and R. Hawig, *IEEE Trans. Magn.* **27**, 3588 (1991).
- [44] R. Skomski and J. M. D. Coey, *Phys. Rev. B* **48**, 15812 (1993).
- [45] H. W. Chang, W. C. Ou, Y. I. Lee, C. W. Shih, W. C. Chang, C. C. Yang, and C. C. Shaw, *IEEE Trans. Magn.* **53**, 1 (2017).
- [46] Y. Kubota, Y. Fu, X. Wu, and T. F. Ambrose, *IEEE Trans. Magn.* **43**, 2998 (2007).
- [47] P. Tozman, M. Venkatesan, G. A. Zickler, J. Fidler, and J. M. D. Coey, *Appl. Phys. Lett.* **107**, 032405 (2015).
- [48] M. D. Kuz'min, *Phys. Rev. Lett.* **94**, 107204 (2005).